SUPPORTING INFORMATION

High-Throughput Reaction Discovery for Cs-Pb-Br Nanocrystal Synthesis

Ricki Chairil[a], Allison P. Forsberg[b], Richard L. Brutchey[b], and Noah Malmstadt[abc]

Affiliations
[a] Mork Family Department of Chemical Engineering and Materials Science, University of Southern California, 925 Bloom Walk, HED 216, Los Angeles, CA 90089, USA
[b] Department of Chemistry, University of Southern California, 3620 McClintock Ave., SGM 418, Los Angeles, CA 90089, USA
[c] Alfred E. Mann Department of Biomedical Engineering, University of Southern California, 925 Bloom Walk, HED 216, Los Angeles, CA 90089, USA

Contents

S1. Reactor design, validation, and operation

S1.1 Reagent preparation details

Cs$^+$ precursor: To make 1L of 10 mM Cs$^+$ precursor: 1.368 g of Cs_2CO_3 was added to a 1L glass bottle (GL45 cap) containing a magnetic stirbar. Then, 84 mL of oleic acid was added. The mixture was stirred moderately and heated to 120°C, until completely dissolved, approximately 2 h. Finally, 840 mL hexane was added and the precursor was mixed and left to cool to room temperature before use.

Pb^{2+} precursor: To make 1L of 10 mM Pb^{2+} precursor: 1.875 g of PbO was added to a 1L glass bottle (GL45 cap) containing a magnetic stirbar. Then, 84 mL of oleic acid was added. The mixture was stirred moderately and heated to 120°C, until completely dissolved, approximately 2 h. Finally, 840 mL hexane was added and the precursor was mixed and left to cool to room temperature before use.

Br$^-$ precursor: To make 1L of 40 mM Br$^-$ precursor: 19.728 g of TOAB was added to a 1L glass bottle (GL45 cap) containing a magnetic stirbar. Then, 72 mL of oleic acid was added. The mixture was stirred vigorously at room temperature for 2 h. Finally, 900 mL hexane was added and mixed.

S1.2 3D-printed device fabrication

3D-printed resistive elements: 3D-printed resistors were designed using Autodesk Inventor Professional. A typical element is a rectangular prism, measuring 35.56 mm × 16.51 mm × 22.86 mm, with a 1/4"-28 UNF threaded hole on opposite ends of the resistor to connect to the reactor network *via* 1/4" outer diameter IDEX HPLC fittings. The interior channels of the resistors have either circular or square cross-sections, with typical characteristic cross-sectional dimensions of 500-800 μm. To modulate internal length, the channels of the resistor are wound in a serpentine fashion by including 90° bends with radius of curvature = 635 μm. For this study, typical internal lengths of up to 0.6 m with 38 bends could be achieved. Figure S1 shows CAD screenshots of a typical resistor.

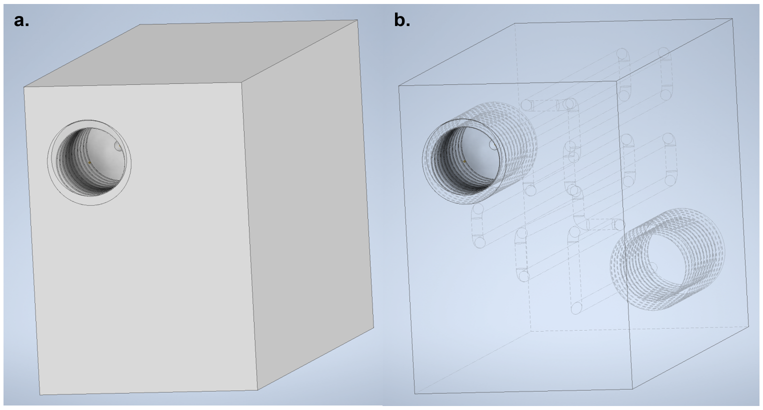

Figure S1. (a) External and (b) internal views of 3D-printed resistor with internal channel diameter = 794 μm, internal length = 41.28 cm, and 26 right-angle bends.

Once designed in Inventor, the resistors were exported as high-quality STL files and printed using a MAX X27 digital light processing (DLP) 3D printer (Asiga; Sydney, Australia) with 50 μm slice thickness. The resin used was clear Printodent GR-10 from Pro3dure Medical GmbH (Iserlohn, Germany). Freshly printed devices were quickly rinsed in several baths of pure isopropanol, and the channels were thoroughly rinsed with clean IPA, to remove excess uncured resin.

Flow distribution manifolds: The 1:4 flow distribution manifolds were used to split the inlet reagent stream into four streams, and then each of those into four additional, for a total of 16 streams. The manufacturing process for these manifolds is described in Wang *et. al.*[11]; they were used here without modification.

Optical detection holding unit: The four-port holder for the fiber-optic cables used for optical detection was mounted on a linear stage and was 3D-printed by Protolabs (Maple Plain, MN, USA) from RenShape SL 7820 photoresin as previously described[11], and was used here without modification.

S1.3 Flow Configuration and Geometry

PEEK tubing of inner diameters 508, 762, and 1575 μm were purchased from McMaster-Carr (Elmhurst, IL, USA). PEEK T-junctions with ID 508 μm through-holes were purchased from IDEX Health & Science (Northbrook, IL, USA). Figure S2 shows a detailed layout of the reactor.

Referring to Figure 1 in the main text, the tubing configuration used throughout this study for the three reagent streams is as follows:

- For all reagents: D_{in} = 1588 μm, L_{in} = 590 mm.
- For all reagents: $D_{out1,i}$ = 1588 μm, $L_{out1,i}$ = 150 mm for all $i \in 1, 2, 3, 4$
- For Br^- stream only: $D_{out2,j}$ = 1575 μm in channels j = 1, 5, 9, 13; 762 μm in channels j = 2, 3, 10, 11, 14, 15; and 508 μm in channels j = 4, 8, 12, 16. $L_{out2,j}$ = 75 mm upstream of resistor, plus another 75 mm downstream of resistor for all $j \in 1, 2, ...16$. This asymmetric arrangement minimizes the effect of maldistribution which can occur when there is insufficient absolute resistance in certain channels of the parallel flow.[8] This was the same reasoning for increasing the resistance throughout the reactor network by using very small (178 μm) ID PEEK tubing in our previous study[11] and elsewhere.[9]
- For Cs^+ and Pb^{2+} streams: $D_{out2,j}$ = 762 μm, $L_{out2,j}$ = 150 mm for all channels $j \in 1, 2, ...16$

As in Wang *et al.*[11], in-line check valves from IDEX were installed directly downstream of the inlet reagent tubing, and compressed nitrogen gas (3-4 bar) was supplied to an MFCS-EZ multichannel pressure regulator (Fluigent; Le Kremlin-Bicêtre, France). This regulator could then be controlled by computer software (Fluigent A-i-O) to set the individual reagent pressures (ΔP in Figure 1 in the main text).

S1.4 *In situ* product monitoring and control systems

The in-line spectral acquisition process follows Wang *et al.* closely[11], except that the IR and self-optimization modules were not required for this present work. All code used can be found on Github: `https://github.com/rchairil/HTS-16-Ch-Reactor`. Briefly, the DH-2000-BAL deuterium/halogen light source (Ocean Insight; Orlando, FL), 405 nm light source (M405FP1 from Thorlabs; Newton, NJ, USA), and portable Flame spectrophotometer outfitted with 200 μm slit (Ocean Insight; Orlando, FL, USA) remained the same. Single SMA-SMA fiber optic patch cables of various core sizes (M92L01, 200 μm; M114L01, 600 μm; M93L01, 1500 μm), as well as an improved 1-to-4 fan-out cable (BF46HS01) with 600 μm core, were obtained from Thorlabs. The core sizes were increased in these cables relative to those in our previous work (which used 200 μm throughout) in order to improve spectral resolution at light wavelengths close to the fiber optic cable limit of 300 nm. The

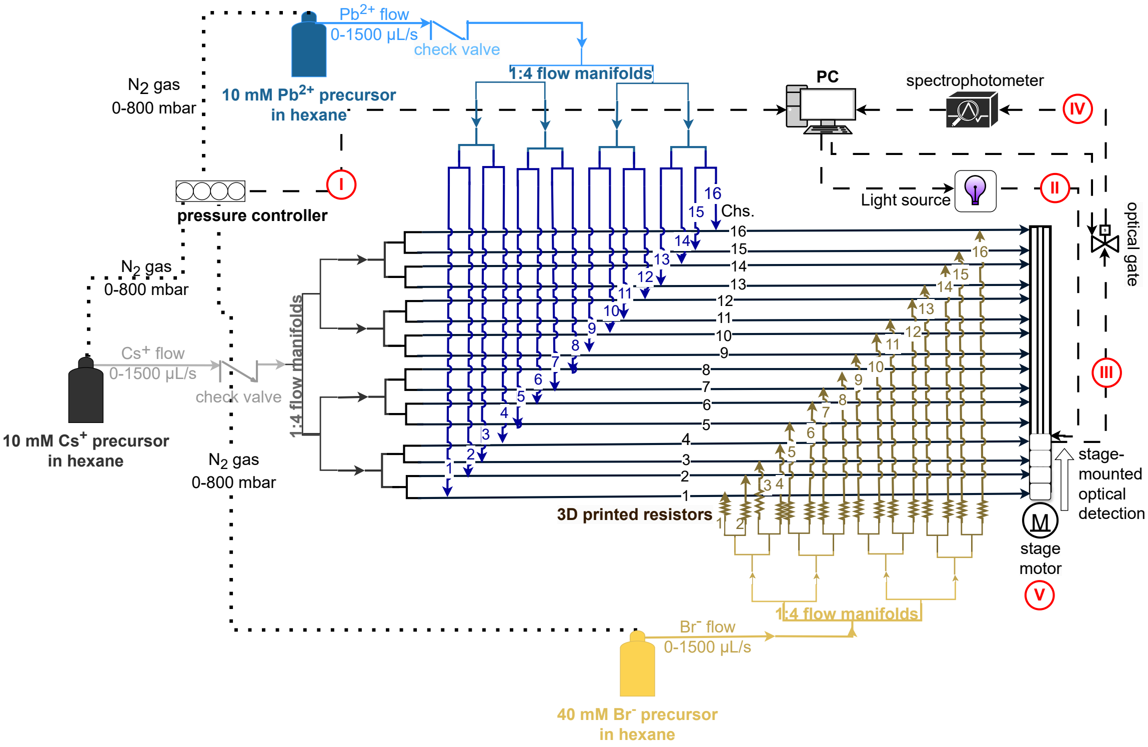

Figure S2. Schematic of the 16-channel HT reaction discovery reactor and auxiliary equipment, where solid lines (—) indicate liquid flows, dotted (...) lines pressurized nitrogen gas, and dashed(- - -) lines information streams. (I) Input pressures for each of the three reagents are specified to the system; after product is formed, white and 405 nm light (II) are flashed onto the first 4 channels of the reactor in sequence, (III) transmitted through the sample and passes an optical gate before going through (IV) the UV-Vis spectrophotometer for spectral analysis, afterwards (V) the linear stage moves to the next block of four channels and the spectral acquisition is repeated until all 16 channels are read.

optical switches, light cages, and solenoids were the same as previously described[11], and were obtained from Thorlabs and SparkFun (Boulder, CO, USA). The stage mount for the optical unit was obtained from Thorlabs. Arduino boards (Uno R3, Mega 2560 R3) remained the same as previously described, and were obtained from SparkFun. Linear stage (MOX-06-400) was obtained from Optics Focus (Beijing, China).

The process of obtaining product spectra is a simplified version of that described in Wang *et al.* As done previously, Python scripts were run to control the linear stage, 405 nm and white light sources, and spectrophotometer. A typical run proceeds as follows:

i. Reagent bottles are filled with desired reagents, and connected to a nitrogen tank *via* the Fluigent pressure system pressurized to 3-4 bar.

ii. Operator opens Fluigent software and sets desired channel pressures, and connects light source, linear stage, and optical gates to respective Arduino boards. Spectrophotometer is also connected to computer.

iii. If not done already, the mounted optical detection unit is manually positioned so that it is as close as possible to the reactor tubing, and so that incident light from the light sources pass through the reactor tubing on the product side.

iv. Operator runs `mrf_405.py` on command prompt or other suitable environment. This script relies on `arduino_control.py` which controls the linear stage movement direction and speed, white and 405 nm light source and shutters, and automated timing of opening/closing the optical gates, all *via* connections to Arduino controller boards. Furthermore, the referenced file `flames_s.py` is also required to control the spectrophotometer, which is connected to the computer using a micro-USB cable.

v. `mrf_405.py` will prompt the operator to check that the linear stage is in its initial position, which is in "block" number 1, in this case, on the furthest-left reactor channel (one "block" is equivalent to four channels, the maximum number of consecutive adjacent channels the optical detector can scan and analyze without moving the stage; in total there are 4 blocks for the 16 channels). If this is not the case, the user inputs the number of blocks to revert the optical unit, and the stage (*via* custom stage movement module of `arduino_control.py`) will automatically jog the unit back by that number of reactor blocks.

vi. Operator powers on the Fluigent flow controller. The three reagents begin flowing and reacting. To allow for steady state, the script instructs the system to wait 45 seconds before collecting spectra. This wait time can be changed as needed.

vii. White light flashes through the reactor tubing product stream for channel 1 and the first optical gate opens; the transmitted light enters the spectrophotometer which records the resulting intensity. The white light shutter closes and the violet 405 nm light is flashed next. The emitted light is transmitted to the spectrophotometer. The first optical gate closes and the second one opens, then the cycle repeats (white light → violet light) until the end of the block is reached.

viii. At the end of the block, the stage moves to the next block, and the spectral acquisition process repeats. This continues until all 16 channels have been read.

ix. The spectrometer reports transmitted light intensity, but does not automatically correct for the absorbance from background. To obtain blanked absorbance values A_j for channel j, the entire procedure above is repeated using solvent only (hexane with 0.317

M oleic acid). Then, we use the equation

$$A_j = \log\left(\frac{I_{blk,j}}{I_{spl,j}}\right) \tag{S1}$$

where $I_{blk,j}$ is the transmitted light intensity of the blank for channel j, and $I_{spl,j}$ is the transmitted intensity for channel j.

S2. Validation processes

S2.1 Flow rate testing w/resistors

Every resistor designed and printed undergoes a simple flow rate test to verify its actual fluid resistance. First, the 3D-printed devices were connected to one channel of the Fluigent pressure distributor, using inlet and outlet tubing segments with known diameter and length. Inert solvent of comparable kinematic viscosity to the Cs-Pb-Br reagents ($\nu \sim$ 0.7-1.0 mm^2/s) for example, isopropanol or ethanol in hexane, etc. was flowed through the resistor at various pressures. The outlet fluid was collected in a graduated cylinder for 70-140 seconds and timed with a stopwatch, which yields an experimental flow rate $\dot{V}$. Thus, applying the Hagen-Poiseulle equation to the system:

$$\frac{\Delta P}{\dot{V}} = R_{in} + R_{res,j} + R_{out} \rightarrow R_{res,j} = \frac{\Delta P}{\dot{V}} - \frac{CL_{in}}{D_{in}^4} - \frac{CL_{out}}{D_{out}^4} \tag{S2}$$

where:

- ΔP = pressure at inlet
- $\dot{V}$ = volumetric flow rate
- R_{in} = fluid resistance of inlet tubing for test setup
- $R_{res,j}$ = fluid resistance of 3D-printed resistor, for channel j
- R_{out} = fluid resistance of outlet tubing for test setup
- C = Hagen-Poiseulle viscosity constant = $\frac{128\mu}{\pi}$ with μ = fluid dynamic viscosity
- L_{in}, D_{in} = length and diameter of inlet tubing, respectively
- L_{out}, D_{out} = length and diameter of outlet tubing, respectively.

S2.2 Theoretical network concentration ratio calculations

Once the experimental resistance of each resistor is evaluated, the mole ratio of every reagent for each of the 16 channels can be predicted. Starting backwards from the definitions of the desired mole ratios $x_{j,k}$ for channel j and reagent k:

$$x_{j,k} = \frac{c_k \dot{V}_{j,k}}{\sum_{k=1}^{3} c_k \dot{V}_{j,k}} \tag{S3}$$

$$k \in \{1, 2, 3\}; j \in \{1, 2, ..., 16\}$$

with:

- c_k = concentration of reagent k
- $\dot{V}_{j,k}$ = volumetric flow rate for channel j, reagent k

Let reagent $k = 1$ be Cs, $k = 2$ be Pb, and $k = 3$ be Br. Then, because the concentration of each reagent is known (see Section S1.1), the only unknowns are the individual channel flow rates.

To predict the flow rates, the Hagen-Poiseulle relation can be applied to the parallel flow reactor network [2]: first, between the pressurized reagent inlet and the split from one stream to four, and again, between the split from four streams to sixteen. Figure 1 in the main text depicts one of the reagent flow networks. Because we have arbitrarily chosen to install the resistors in the Br^- stream, first consider the case where k = 3. Then, because the reactor tubing carries its own resistance to flow, the Ohm's Law-type relationship for flow resistors in parallel for the first split gives:

$$\dot{V_{i,3}} = \frac{\frac{1}{R_{i,3}}}{\sum_{l=1}^{4} \frac{1}{R_{l,3}}} \frac{\Delta P}{CL_{in}/D_{in}^4} \tag{S4}$$

where:

- $\dot{V_{i,3}}$ = volumetric flow rate for Br^-, channel i (from 1 to 4)
- $R_{i,3}$ = total fluid resistance of channel i

In the vicinity of this first split (bounded by the violet box in Figure 1), the fluid resistance $R_{i,3}$ is simply equal to the resistance R_M of the first 1:4 flow manifold channels, plus that associated with the connecting tubing leading out of this first manifold.

Next, the Hagen-Poiseulle relation is applied again to the second split:

$$\dot{V_{j,3}} = \frac{\frac{1}{R_{j,3}}}{\sum_{m=4i-3}^{4i} \frac{1}{R_{m,3}}} \dot{V_{i,3}} \tag{S5}$$

$$j \in \{1, 2, ..., 16\}; i \in \{1, 2, 3, 4\}$$

where $\dot{V_{j,3}}$ is the volumetric flow rate of bromide reagent for channel j. Here, because the flow in each downstream channel j depends on its parent stream i, if j = 1, 2, 3, or 4, i must be equal to 1; if j = 5, 6, 7, 8, i must be equal to 2; and so on until j = 13 to 16 (i = 4). The region of the flow reactor where Eq. S5 applies is defined by the light blue box in Figure 1. In essence, the flow rate in channel j depends on the resistances in its three other connected neighbors.

Combining Equations S4 and S5, we have:

$$\dot{V_{j,3}} = \frac{\frac{1}{R_{j,3}}}{\sum_{m=4i-3}^{4i} \frac{1}{R_{m,3}}} \frac{\frac{1}{R_{i,3}}}{\sum_{l=1}^{4} \frac{1}{R_{l,3}}} \frac{\Delta P}{CL_{in}/D_{in}^4} \tag{S6}$$

$$j \in \{1, 2, ..., 16\}; i \in \{1, 2, 3, 4\}$$

Now, note that the individual resistance in channel j can be described as a series of sub-"resistors", and equal to:

$$R_{j,3} = R_{res,j} + R_{out2,j} \tag{S7}$$

where $R_{out2,j} = CL_{out2,j}/D_{out2,j}^4$ is the total resistance associated with the tubing connecting the second manifold to the 3D-printed resistor, plus that of the tubing from the 3D-printed resistor down to the product outlet. Therefore, combining Equations S6, S3, and S2 directly link the 3D-printed design resistance to the theoretical mole ratio of Br^-, $x_{j,3}$. To get $x_{j,1}$ and $x_{j,2}$ is a simpler task; since there are no 3D-printed resistors installed in those streams, the $R_{res,j}$ term in Equation S7 is omitted, then Equations S6 and S3 can be applied to calculate a theoretical mole ratio. Finally, a simple solvent flow rate measurement (as described in Section 3.1 in the main text), but throughout the entire 16-channel reactor with resistors installed, can be used to obtain the actual mole ratios, which are compared to these theoretical predictions. The mole ratios for $k = 3$ (Br^-) depicted in Figure 2(c) in the main text were obtained this way.

S2.3 3D-printed resistor statistical model

To further emphasize the effect of design on resistor resistance, a predictive model in Minitab was created. This model maps the resistance of a 3D-printed resistor given its characteristic channel size or diameter, input pressure, channel length, and number of rectilinear bends. In total, the experimental flow data collected from 27 unique resistor designs of varying geometries and pressures ranging from 50-800 mbar were used to build this model, representing a total of 157 design-pressure combinations. A third-order response surface with up to third-order interactions was included; statistically-significant terms were added to the model *via* the backward elimination method with cutoff $\alpha = 0.05$. The resulting model details are shown in Figure S3.

a.

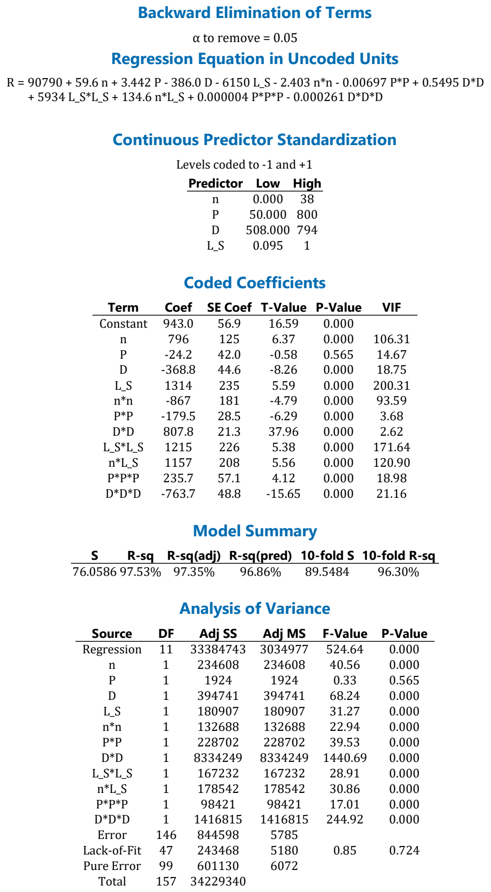

Backward Elimination of Terms

α to remove = 0.05

Regression Equation in Uncoded Units

R = 90790 + 59.6 n + 3.442 P - 386.0 D - 6150 L_S - 2.403 n*n - 0.00697 P*P + 0.5495 D*D
+ 5934 L_S*L_S + 134.6 n*L_S + 0.000004 P*P*P - 0.000261 D*D*D

Continuous Predictor Standardization

Levels coded to -1 and +1

Predictor	Low	High
n	0.000	38
P	50.000	800
D	508.000	794
L_S	0.095	1

Coded Coefficients

Term	Coef	SE Coef	T-Value	P-Value	VIF
Constant	943.0	56.9	16.59	0.000	
n	796	125	6.37	0.000	106.31
P	-24.2	42.0	-0.58	0.565	14.67
D	-368.8	44.6	-8.26	0.000	18.75
L_S	1314	235	5.59	0.000	200.31
n*n	-867	181	-4.79	0.000	93.59
P*P	-179.5	28.5	-6.29	0.000	3.68
D*D	807.8	21.3	37.96	0.000	2.62
L_S*L_S	1215	226	5.38	0.000	171.64
n*L_S	1157	208	5.56	0.000	120.90
P*P*P	235.7	57.1	4.12	0.000	18.98
D*D*D	-763.7	48.8	-15.65	0.000	21.16

Model Summary

S	R-sq	R-sq(adj)	R-sq(pred)	10-fold S	10-fold R-sq
76.0586	97.53%	97.35%	96.86%	89.5484	96.30%

Analysis of Variance

Source	DF	Adj SS	Adj MS	F-Value	P-Value
Regression	11	33384743	3034977	524.64	0.000
n	1	234608	234608	40.56	0.000
P	1	1924	1924	0.33	0.565
D	1	394741	394741	68.24	0.000
L_S	1	180907	180907	31.27	0.000
n*n	1	132688	132688	22.94	0.000
P*P	1	228702	228702	39.53	0.000
D*D	1	8334249	8334249	1440.69	0.000
L_S*L_S	1	167232	167232	28.91	0.000
n*L_S	1	178542	178542	30.86	0.000
P*P*P	1	98421	98421	17.01	0.000
D*D*D	1	1416815	1416815	244.92	0.000
Error	146	844598	5785		
Lack-of-Fit	47	243468	5180	0.85	0.724
Pure Error	99	601130	6072		
Total	157	34229340			

b.

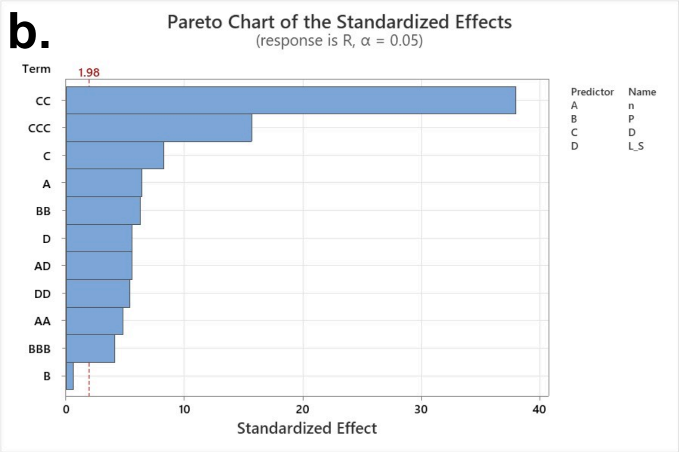

Figure S3. (a) Minitab predictive model for 3D-printed resistance as a function of geometry and input pressure, alongside goodness of fit and ANOVA details. The predictors are: n (number of 90-degree bends), P (input pressure in mbar), D (channel characteristic size in μm), and L_S (internal channel length in m). (b) Pareto chart of significant effects and interactions: A = number of 90-degree bends, B = input pressure, C = channel size, D = internal channel length.

As seen in Figure S3a, pressure was identified as a non-significant parameter for flow resistance, highlighting the applicability of the Hagen-Poiseulle flow to our reactor network as indicated in Figure 2b of the main text. Despite this, the first-order pressure term is still included in the final predicted response surface to maintain the hierarchical properties of the model.

S2.4 Machine learning process

This section details the machine learning (ML) optimization and prediction process. Figure S4 summarizes the workflow. All ML models were run from Scikit-learn packages in Python.[10] Three different ML classifiers were used in order to obtain a more holistic understanding of the predicted product phase frontiers. The ML classifiers employed were:

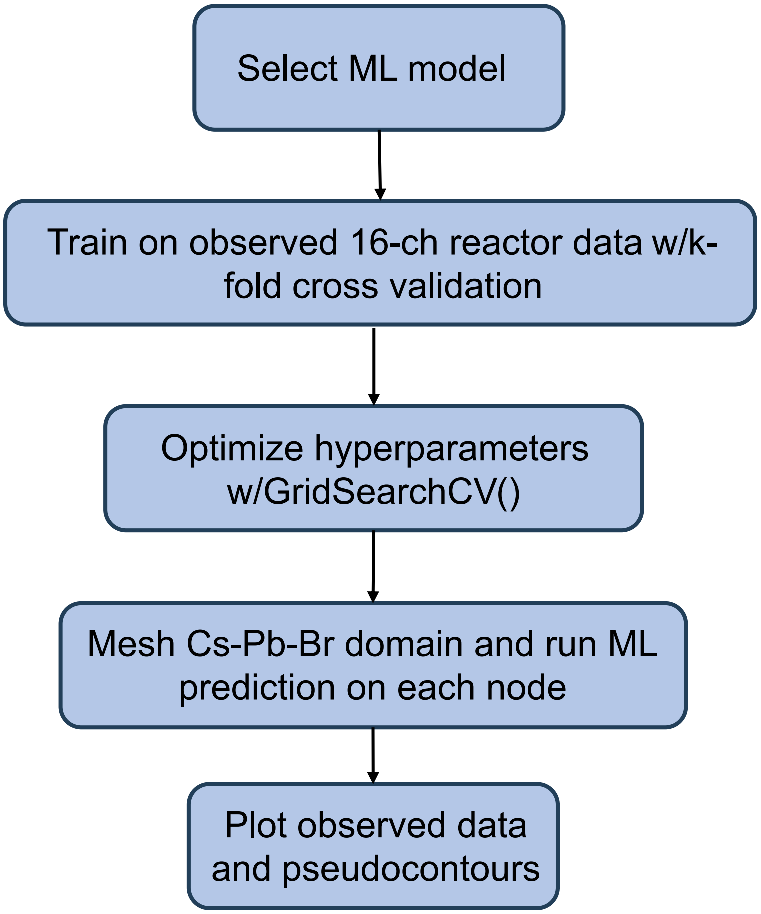

Figure S4. Machine learning workflow for prediction and pseudocontouring of unknown Cs-Pb-Br mole ratios, based on observed screening data.

- `KNeighborsClassifier()`: k-nearest neighbors method[13]
- `SVC()`: support vector classifier[3]
- `MLPClassifier()`: multi-layer perceptron neural network [4]

The code for all three ML models is available on Github (`https://github.com/rchairil/HTS-16-Ch-Reactor`) and are named `ternary_XXX.py` where `XXX` is the ML method used

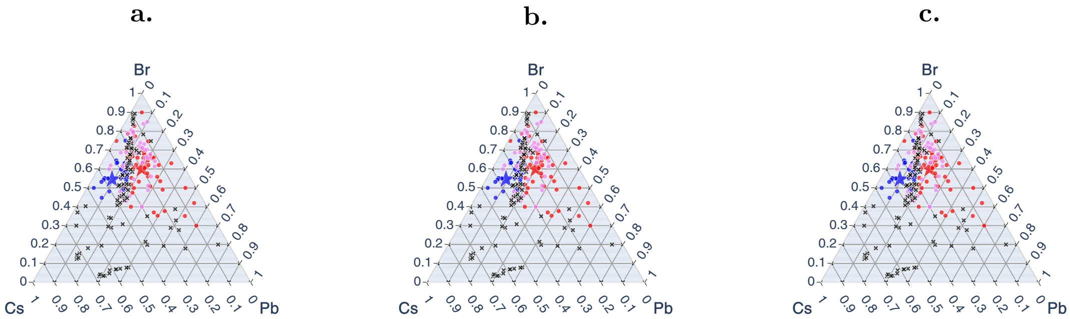

Figure S5. Observed data points and ML-predicted product phases for (a) k-neighbors classifier, (b) support vector classification, and (c) multi-layer perceptron neural network. Legend - Observed data: ● $CsPbBr_3$; ● Cs_4PbBr_6; ● coexistence of $CsPbBr_3$ and Cs_4PbBr_6), **X** = neither phase/no reaction; stoichiometric centers: ★ $CsPbBr_3$, ★ Cs_4PbBr_6; ML predictions: - $CsPbBr_3$; - Cs_4PbBr_6; - coexistence of $CsPbBr_3$ and Cs_4PbBr_6, - neither phase/no reaction

(`KNC`, `SVC`, or `MLP`). As shown in Figure S4, each ML model was first trained on the observed product phase data from the 16-channel reactor, with pressures and installed resistors manipulated to produce certain Cs-Pb-Br ratios. The absorbance and PL spectra were then inspected, and confirmatory XRDs taken as needed (see Section S3), and the product for each observed data point is categorized into $CsPbBr_3$, Cs_4PbBr_6, a coexistence of $CsPbBr_3$ and Cs_4PbBr_6, or neither phase/no reaction. From there, a 10-fold cross validation process with 3 repeats (30 folds total) was performed in order to mitigate the dependence of the models' performance on the specific train/validation split. The hyperparameters were optimized using the `GridSearchCV()` function in Scikit-learn. Then, the entire Cs-Pb-Br ternary domain was meshed into approximately 500,000 individual data nodes, with each node representing a mole ratio of $x_{Br} : x_{Cs} : x_{Pb}$. The trained and optimized ML model was then tasked with predicting the most-likely product phases for those ∼500,000 nodes. The resulting contours are shown in Figure S5.

The optimized hyperparameters of note are as follows:

- `KNeighborsClassifier(): leaf_size = 2, n_neighbors = 13, weights = ’uniform’`
- `SVC(): C = 1.067, degree = 5, kernel = poly`
- `MLPClassifier(): hidden_layer_sizes = (75,), activation = ’relu’, solver = ’lbfgs’, learning_rate=’constant’, max_iter = 2000`

Finally, as a metric for goodness of model fit, the learning curves for each ML model were obtained; they are shown in Figure S6.

We note that the average model accuracy for MLP is the highest (60%) among the three ML models chosen. Therefore, MLP was chosen as the optimal model to predict the most-likely product phases based on the screening data.

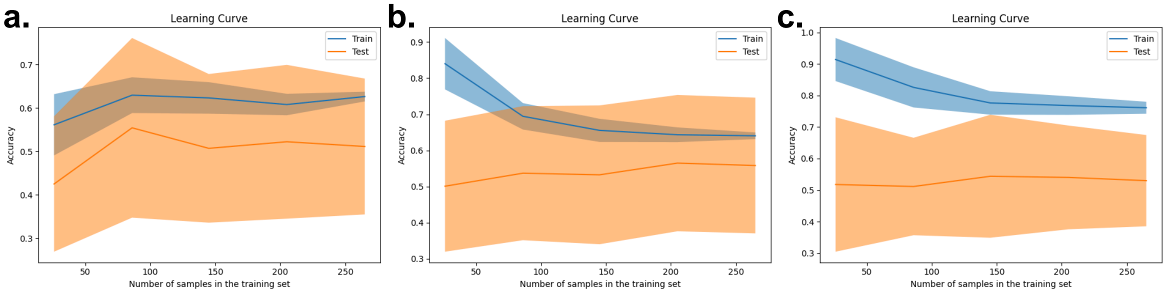

Figure S6. Validation learning curves for (a) k-neighbors classifier, (b) support vector classification, and (c) multi-layer perceptron neural network.

S2.5 Evaluation of inherent flow variability in the 16-channel reactor network

Differences in mixing efficiency: In any parallel flow configuration, the degree of mixing will inevitably vary between channels. Falk and Commenge provide theoretical mixing times as a function of the Peclet number (Pe), or the ratio of advective to diffusive transport. This mixing time t is given in Equation S8[6]:

$$t = \frac{d^2/\mathcal{D}}{8Pe} \ln{(1.52Pe)} \tag{S8}$$

where d = channel diameter, $\mathcal{D}$ = diffusion coefficient, and Pe = the Peclet number of the flow. The Peclet number can also be recast in terms of the Reynolds (Re) and Schmidt (Sc) numbers, $Pe = ReSc$. Using a Schmidt number of approximately 116 for hexane at 25°C[7], average reactor diameter of 800 μm, hexane diffusivity $\mathcal{D} = 4.2 \cdot 10^{-9}\ m^2\ s^{-1}$, and given that the 16-channel reactor typically operates between $Re = 300$ and $Re = 1300$, we calculate from Equation S8 mixing times on the order of 2 - 6 ms. The typical residence times produced by the reactor, based on flow rate data, are 0.5 - 2 s. Thus, in the worst case, less than 1.2% of the reactor residence time is required for adequate mixing throughout the 16 channels, i.e. the relatively quick mixing times obviate the need to consider differences in mixing efficiency between channels. Furthermore, the precursors are introduced to each other in cross-flow through T-junctions, which further promote mixing.

Differences in fluid resistance due to particle precipitation: Another potential source of inherent reactor flow variability is the increase in flow resistance caused by the nanocrystal particles as they precipitate out of solution. Consider a reaction where the maximum concentration (10 mM) of precipitated product, either $CsPbBr_3$ or Cs_4PbBr_6, instantaneously forms in the flow reactor channels. This concentration corresponds to a bulk solid particle concentration of 5.8 g/L for $CsPbBr_3$ or 12.2 g/L for Cs_4PbBr_6. Using the densities of $CsPbBr_3$ = 4.8 g/mL and Cs_4PbBr_6 = 4.2 g/mL, the maximum solid volume fraction φ = (solid volume)/(total volume) can be calculated as 0.003 (0.3%). The apparent viscosity increase, when $\varphi < 0.02$, can thus be expressed as[1]:

$$\frac{\mu *}{\mu} = 1 + 5\varphi/2 \tag{S9}$$

where $\mu * /\mu$ is the ratio of the particle suspension dynamic viscosity to that of the particle-free bulk fluid. In the worst case, when $\varphi = 0.003$, this ratio is only equal to 1.008, meaning that the maximum possible increase in flow resistance due to precipitation is less than 0.8%. Thus, changing fluid resistances due to particle production was deemed negligible. In addition, after every run, all streams were thoroughly flushed with hexane to minimize particle buildup on the channel interior walls.

S3. Supporting data for product identification and analysis

S3.1 Exclusion of metastable $CsPb_2Br_5$ as product

The metastable $CsPb_2Br_5$ is a phase that has been reported as a potential metal halide perovskite (MHP)-like product for this Cs-Pb-Br system.[5] It is characterized by a strong narrow absorbance peak around 325 nm, the absence of excitonic edge around 450-500 nm, and pronounced fluorescence emission maximum (excitation at 405 nm) around 500 nm.[5] This phase was not observed in any of the experimental trials on the basis of absorbance/PL, and also from XRD as seen in Figure S7, which was taken from a sample with ternary mole ratio coordinates corresponding to the stoichiometry of $CsPb_2Br_5$. The presence of $CsPb_2Br_5$ was not observed; rather, a coexistence of $CsPbBr_3$ and Cs_4PbBr_6 is obtained instead, likely due to these two species being more thermodynamically favored.[12]

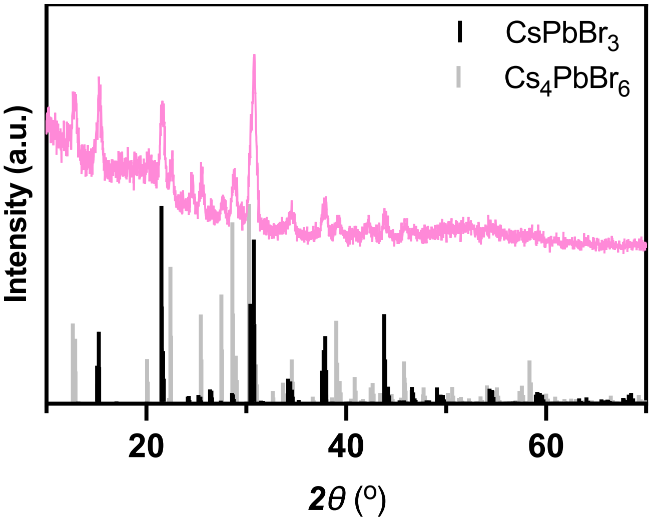

Figure S7. Typical post-washed powder XRD for coexistence of $CsPbBr_3$ and Cs_4PbBr_6 (Cs-Pb-Br mole ratios = (0.13, 0.25, 0.62)), with reference sticks in black and gray for $CsPbBr_3$ and Cs_4PbBr_6 respectively. Samples were washed in toluene per the Experimental section in the main text. Note that the reference stick pattern for $CsPb_2Br_5$ is not shown as the experimental XRD trace indicates the presence of only $CsPbBr_3$ and Cs_4PbBr_6, rather than $CsPb_2Br_5$.

S3.2 Validation of ML predictions for small batch reactions

To further demonstrate the applicability of the product phase predictions, small batch reactions (3 mL each) were performed and characterized off-line. These batch reactions were carried out at the same five external validation concentration ratios chosen from Figure 4 in the main text. As indicated in Figure S8, the absorbance, fluorescent photoluminescence, and X-ray diffraction patterns of these batch reactions all align with the ML predictions given in the main text, showing the validity of this ML model for both batch and flow syntheses.

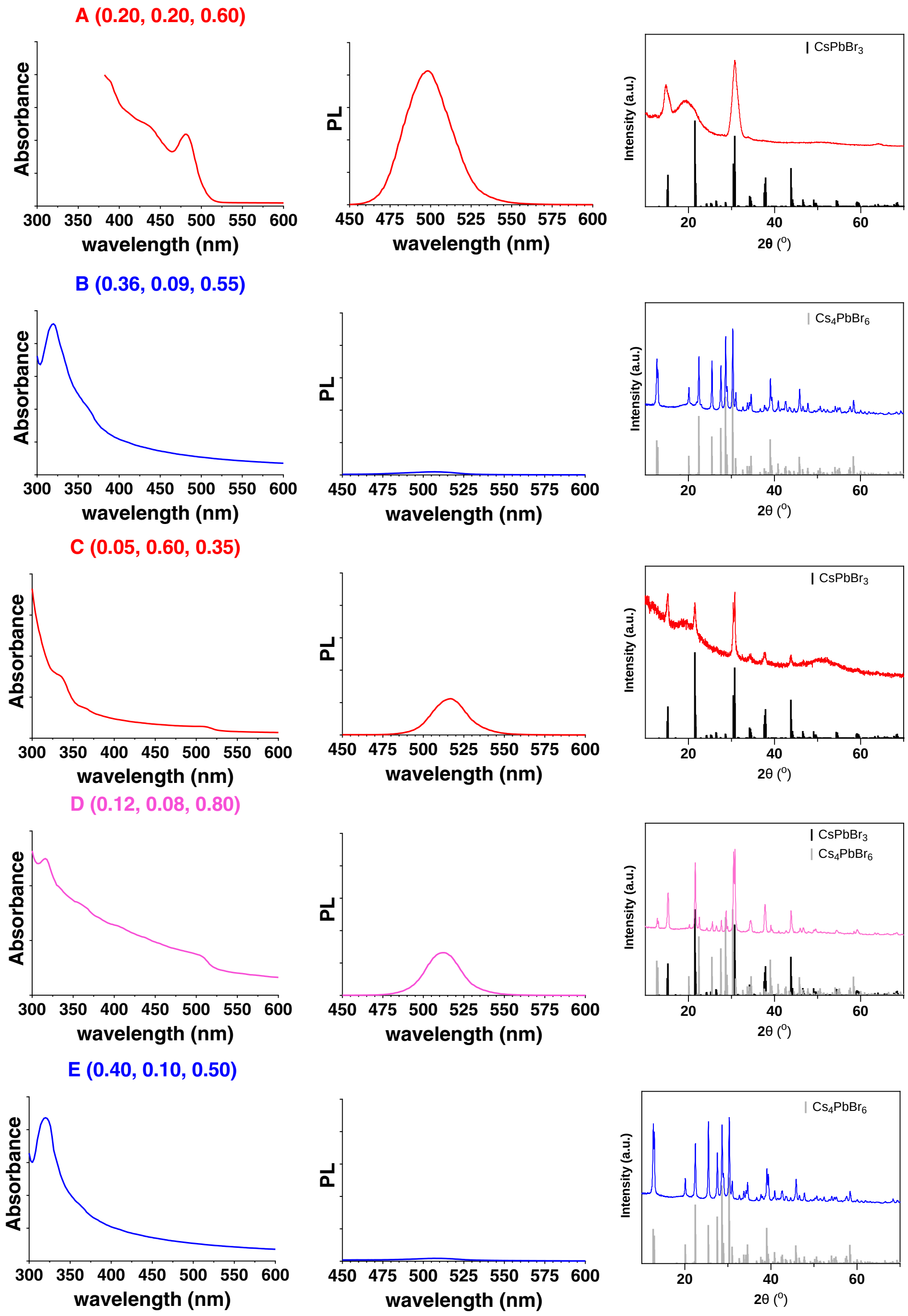

Figure S8. Characterization data for the external validation points from Figure 4 in the main text, performed in 3 mL batch reactions. First column from the left = UV-Vis absorbance spectra; second column = PL from excitation λ_{ex} = 405 nm; third column = experimental XRD traces in red, blue, or pink (reference XRD sticks for CsPbBr$_3$ and Cs$_4$PbBr$_6$ are shown in black and gray respectively).

References

[1] G. K. Batchelor. The effect of brownian motion on the bulk stress in a suspension of spherical particles. *J. Fluid Mech.*, 83(1):97–117, 1977.

[2] K. C. Bhargava, B. Thompson, D. Iqbal, and N. Malmstadt. Predicting the behavior of microfluidic circuits made from discrete elements. *Sci. Rep.*, 5(1):15609, Oct 2015.

[3] C.-C. Chang and C.-J. Lin. Training v-support vector classifiers: Theory and algorithms. *Neural Comput.*, 13(9):2119–2147, 2001.

[4] S. Curteanu and H. Cartwright. Neural networks applied in chemistry. i. determination of the optimal topology of multilayer perceptron neural networks. *J. Chemom.*, 25(10):527–549, 2011.

[5] J. C. Dahl, X. Wang, X. Huang, E. M. Chan, and A. P. Alivisatos. Elucidating the weakly reversible cs–pb–br perovskite nanocrystal reaction network with high-throughput maps and transformations. *J. Am. Chem. Soc.*, 142(27):11915–11926, 2020. PMID: 32531162.

[6] L. Falk and J.-M. Commenge. Performance comparison of micromixers. *Chem. Eng. Sci.*, 65(1):405–411, 2010. 20th International Symposium in Chemical Reaction Engineering—Green Chemical Reaction Engineering for a Sustainable Future.

[7] K. R. Harris. Temperature and density dependence of the self-diffusion coefficient of n-hexane from 223 to 333 k and up to 400 mpa. *J. Chem. Soc., Faraday Trans. 1*, 78:2265–2274, 1982.

[8] J. M. Hassan, T. A. Mohamed, W. S. Mohammed, and W. H. Alawee. Modeling the uniformity of manifold with various configurations. *J. Fluids*, 2014:325259, Aug 2014.

[9] A. M. Nightingale, J. H. Bannock, S. H. Krishnadasan, F. T. F. O'Mahony, S. A. Haque, J. Sloan, C. Drury, R. McIntyre, and J. C. deMello. Large-scale synthesis of nanocrystals in a multichannel droplet reactor. *J. Mater. Chem. A*, 1:4067–4076, 2013.

[10] F. Pedregosa, G. Varoquaux, A. Gramfort, V. Michel, B. Thirion, O. Grisel, M. Blondel, P. Prettenhofer, R. Weiss, V. Dubourg, J. Vanderplas, A. Passos, D. Cournapeau, M. Brucher, M. Perrot, and E. Duchesnay. Scikit-learn: Machine learning in Python. *J. Mach. Learn. Res.*, 12:2825–2830, 2011.

[11] L. Wang, L. R. Karadaghi, R. L. Brutchey, and N. Malmstadt. Self-optimizing parallel millifluidic reactor for scaling nanoparticle synthesis. *Chem. Commun.*, 56:3745–3748, 2020.

[12] Y. Yin, Y. Liu, G. Cao, Z. Lv, H. Zong, Y. Cheng, Q. Dong, C. Liu, M. Li, and B. Zhang. Optical properties and mechanical induced phase transition of cspb2br5 and cspbbr3 nanocrystals. *J. Alloys Compd.*, 947:169439, 2023.

[13] Z. Zhang. Introduction to machine learning: k-nearest neighbors. *Ann. Transl. Med.*, 4(11), 2016.